

Cite this: DOI:[10.56748/ejse.25667](https://doi.org/10.56748/ejse.25667)Received Date: 27 July 2024
Accepted Date: 22 February 2025

1443-9255

<https://ejsei.com/ejse>Copyright: © The Author(s).
Published by Electronic Journals
for Science and Engineering
International (EJSEI).
This is an open access article
under the CC BY license.<https://creativecommons.org/licenses/by/4.0/>

Mesoscale numerical study of size effect on concrete fracture characteristics based on FDEM

Yamin WU ^{a*}, Tuanjie WANG ^{a,b}, Junfeng DUAN ^a, Lei SONG ^c^a School of Architectural Engineering, Zhengzhou University of Industrial Technology, Xinzheng 451100, China^b College of Environmental Science and Engineering, Nankai University, Tianjin 300350, China^c China Construction Seventh Engineering Division Corp. Ltd., Zhengzhou 450004, China*Corresponding author: wuyamin410@163.com

Abstract

Fracture characteristics of concrete remain a focal point of current research. Traditional experimental approaches and finite element simulations face limitations in the study of concrete fracture behavior. The novel combined finite-discrete element method (FDEM) offers pronounced advantages for investigating concrete fracture at the mesoscopic scale. In this paper, utilizing the FDEM approach, a mesoscale concrete model encompassing aggregates, mortar, and the interfacial transition zone was constructed. Three-point bending simulations on concrete beams with precast cracks revealed the mesoscopic fracture processes and characteristics. Results showed that as beam height increases, the fracture energy of the specimens first increases then decreases, and the ductility index decreases. Additionally, as the crack height ratio increases, the beam's fracture energy gradually lowers, while the ductility index initially rises then falls. This study provides insights into beam fracture mechanisms and properties, contributing to the failure analysis of concrete structures at the engineering scale.

Keywords

Concrete, Microscopic simulation, Fracture characteristic, FDEM, Size effect

1. Introduction

Concrete is the most extensively used construction material in the world, with broad applications in the field of civil engineering. Understanding its failure mechanisms is critical for ensuring the safety of concrete structures (Yankelevsky 2024). Despite this, the complexity and heterogeneity of its components means that the mechanisms behind concrete failure, specifically under complex stress states, remain inadequately understood. The height of the ligaments directly impacts the fracture process in concrete and the consequent release of energy. This process is influenced by parameters such as the height of the beam and the ratio of crack height to depth. Previous experiments have investigated concrete's size effects: in three-point bending tests of beams, it was observed that the fracture energy of a specimen first increases and then decreases with an increase in beam height (Tang et al. 2022; Yin and Hu 2021). It reduces as the crack height ratio of the specimens increases (Xue et al. 2023; Yin et al. 2023), and the energy released per element length of crack propagation is contingent on the state of the fracture process zone (FPZ) (Yin et al. 2024). For smaller structures, the size effect is predictable, with material randomness defining the statistical distribution of nominal strength (Bažant 2004). However, when sample sizes become too large, the measured energy according to RILEM standards becomes unreliable (Guo and Gilbert 2000). Additionally, conventional testing methods struggle to detect the internal processes and mechanisms driving damage and failure in concrete.

Within the matrices of concrete, a distinctive boundary layer evolves between the aggregate components and the mortar substance, recognized as the Interfacial Transition Zone (ITZ). Residing within the confines of this ultra-thin band, ranging from merely 30 μ m up to 100 μ m, amplifies the inherent difficulty in developing a precise finite element model. Furthermore, the ITZ's strength and elasticity modulus notably fall short in comparison to the mortar. This disparity significantly influences the creation and propagation of fissures in concrete (Chen et al. 2024; Liu et al. 2024; Zhu et al. 2024). At present, the finite element method encounters substantial limitations, hindering its capability to mirror the ITZ's unique geometric structure and its role in inciting and escalating cracks in the specimens. This constraint obstructs the advancement of research exploring the damage and failure mechanisms in concrete, particularly on a microscale. Turning towards the discrete element methods (DEM), a predominant assumption that elements maintain rigidity introduces an additional complexity. To authentically replicate the aggregate's shape and size characteristics, a multitude of elements become obligatory, consequently compromising computational efficiency.

Amidst these challenges, the Finite-Discrete Element Method (FDEM) surfaces as an innovative solution, efficiently addressing the concerns

aforementioned. The strength of FDEM lies in its ability to discretize a region through the integration of cohesive elements positioned amidst solid ones. Employing the discrete element method, contact forces and relative displacements between discrete elements are evaluated, whereas deformation and stress experienced by each discrete body are solved using finite element techniques. This approach facilitates a detailed overview of specimen cracking and failure, depicting them through the damage and annihilation of the cohesive elements. Diverging from traditional fracture mechanics, cohesive elements forego established crack initiation criteria, treating crack propagation as a continuous degradation of the cohesive elements' material properties. As a direct result, this method can substantially alleviate or even eradicate the stress singularities at crack tips. Researchers (Wang and Xu 2024; Zhang Ruilin et al. 2023) formulated homogenized XFEM models for three-point bending beams and equivalent pure bending beams, respectively. Direct comparison of these simulations with experimental studies revealed minor inconsistencies; the simulated peak loads registered marginally higher than the actual experimental outcomes. This discrepancy is attributed to these models' inability to account for the aggregate interlock action. Subsequently, Chen (Chen et al. 2022) went on to devise a mesoscale model, although it unfortunately fell short of illuminating the underlying fracture mechanisms and the influence of size effects.

Building on the foundation of the FDEM method, this study creates several mesoscale concrete models of concrete beam with varying beam depths and different notch-to-depth ratio for three-point bending tests, taking into consideration the ITZ. Numerical simulations for three-point bending tests are performed to gain insights into the mechanisms driving the formation and progression of primary cracks within the concrete beams. The study deliberates on the role aggregates and ITZ play in shaping the evolution of the stress field during crack expansion. Furthermore, an in-depth analysis considers the effects of beam depth and notch-to-depth ratio on several aspects: beam fractures, the P-CMOD curve, fracture energy, and the ductility index. The cumulative findings of this research serve as an essential reference for a thorough understanding of the mechanisms underlying fracture and destruction in concrete structures.

2. Numerical Modeling Method

2.1 Generation of mesoscopic model

The mesoscopic structure of concrete consists of Mortar and randomly distributed aggregates within it. The well-known Walraven formula found on the Fuller curve was applied to compute of the quantity of aggregates featuring a particle size of d_l , positioned anywhere within a

two-dimensional cross-section, as articulated in the ensuing explanation (Ma et al. 2016):

$$N = [p_c(d_{l+1} < d_0) - p_c(d_l < d_0)] \frac{A}{A_l} \quad (1)$$

Where: A represents the planar area of the two-dimensional section. A_l represents the cross-sectional area of aggregate with a particle size of d_l .

The content of aggregates within the mesoscopic model was calculated based on the concrete mix ratio and aggregate gradation. A program to generate and place random polygonal aggregate models was written in Matlab, utilizing the Monte Carlo method. Random polygonal aggregates were placed within the specified two-dimensional area in such a manner that the resultant models satisfied the requirements of non-overlapping and minimum gaps between aggregates. Accordingly, mesoscopic geometric models of concrete with various sizes or proportions were obtained (Figure 1(a)). These geometric model entities were then imported into Abaqus, where Boolean operations were conducted. Different element sets for aggregates and the Mortar were established, followed by meshing, which resulted in the mesoscopic finite element model of the concrete (Fig. 1(b)).

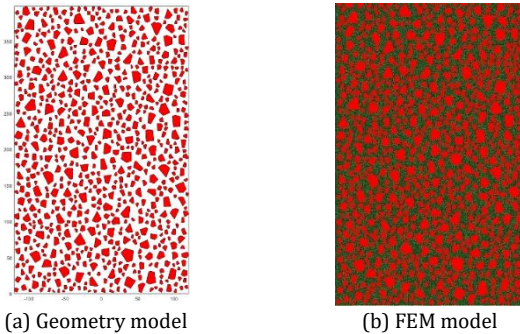


Fig.1 Mesoscale model

In this study, zero-thickness COH2D4 elements in ABAQUS were utilized, and the FDEM was implemented via the user subroutine interface. An explicit dynamic analysis was employed to solve the problem, which effectively avoided convergence issues. After meshing the mesoscopic structure of the concrete, cohesive elements were inserted along every mesh line within the mesoscopic structure using an internally developed code. The general procedure for inserting cohesive elements into such a mesoscopic structure is given by (Zhou et al. 2020), and listed below:

- (1) Acquire the node and element files.
- (2) Read the node coordinates and element arrays and determine the number of entity elements that each shared node belongs to.
- (3) Duplicate the nodes.
- (4) Discretize the entity elements.
- (5) Insert cohesive elements.
- (6) Determine the material types of cohesive elements based on the element sets to which they belong.

Based on the mesoscopic structure of concrete, this study identified three types of interface elements, namely, the mortar-mortar (internal mortar) interface elements, aggregate-mortar interface elements, and aggregate-aggregate interface elements, as shown in Figure 2. This model simulates the formation of cracks by embedding zero-thickness cohesive elements in potential crack regions. It has the ability to simulate the extension and merger of micro-cracks and can capture the entire evolution process of the FPZ (Fracture Process Zone).

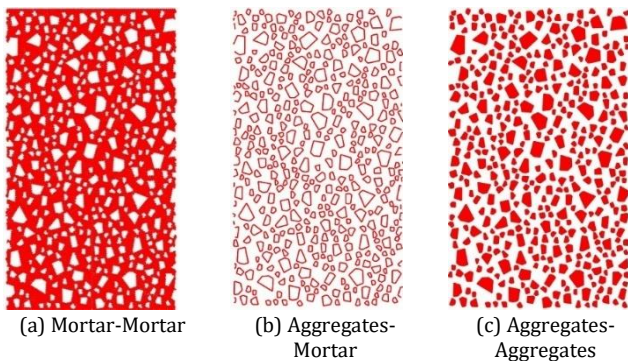


Fig. 2 Cohesive element in mesoscale model

2.2 Constitutive Model

The XFEM model for concrete is composed of triangular solid elements and cohesive elements. The solid elements utilize a linear elastic constitutive model, whereas the constitutive model for the cohesive elements is defined through a combination of traction-separation and

damage evolution. The stress status of the cohesive elements adheres to elastic traction-separation prior to reaching the damage threshold. Upon reaching this threshold, it transitions into the damage evolution stage. This stage persists until the cohesive element surpasses the failure threshold, consequently leading to its removal and the formation of a crack at that specific location.

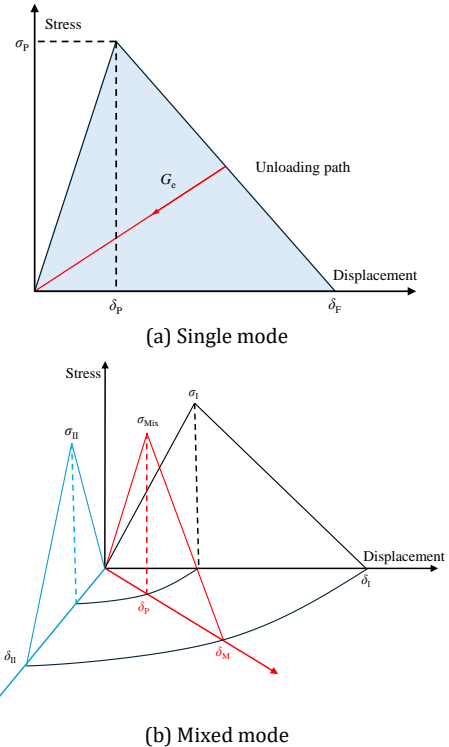


Fig. 3 Cohesive constitutive model

Given that the bilinear model aptly characterizes the fracture behavior of brittle materials and ensures computational efficiency, it has been selected to define the traction-separation relationship for cohesive elements. Figure 3(a) depicts the traction-separation constitutive curve of the bilinear model, featuring a softening segment. The notations δ_p and δ_f denote the initial cracking displacement and the failure displacement, respectively. The fracture energy, G_c , corresponds to the area under the curve bounded by the triangle in the figure. Initially, it is postulated that the relationship between displacement and stress is linear, possessing a stiffness denoted by $K = \sigma_p / \delta_p$. Once the stress attains its peak value, the cohesive element transitions into the softening stage, wherein cracks initiate and extend, accompanied by a monotonic decline in stress with increasing displacement. The element is considered failed and subsequently removed when the stress falls to zero.

In order to characterize the damage arising from the interplay of normal and shear deformation at interfaces, an effective relative displacement, denoted as d_m , has been introduced. The initial onset of damage within a cohesive element is assessed using the squared nominal stress criterion. Point A represents the damage threshold: damage commences within the cohesive element once its nominal stress aligns with Equation (2).

$$\left(\frac{\langle t_n \rangle}{t_n^{max}} \right)^2 + \left(\frac{\langle t_s \rangle}{t_s^{max}} \right)^2 = 1 \quad (2)$$

Where, the variables $\langle t_n \rangle$ and $\langle t_s \rangle$ signify the maximal nominal stresses correspond to pure tensile and pure shear stress conditions, respectively. The Macaulay operator is represented by the angular brackets. Figure 3(b) presents a detailed illustration of the coupling between two independent deformation modes. The terms σ_I , σ_{II} , and σ_{Mix} provide the traction forces associated with the commencement of fracture in pure mode I, pure mode II, and mixed mode, respectively. Correspondingly, δ_I , δ_{II} , and δ_{Mix} denote the associated displacements for these modes. For an in-depth understanding of the coupling relationship between independent Type I and Type II fractures, readers are directed to reference [16].

2.3 Three-Point Bending Simulation Model of Beams

In this study, modeling was conducted on concrete beams with five different beam depths and five different notch-to-depth ratios. The span-to-depth ratio S/D of all specimens was set as 4, with the thickness B as 40 mm. The details of the numerical model setup are illustrated in Figure 4. Previous empirical studies (Wu et al. 2011) and numerical calculations (Zhou and Chen 2019) have consistently indicated that damage is localized near the notch area, while the rest of the beam remains mostly undamaged

throughout the entire loading process. Consequently, the "multi-scale" approach adopted in this paper focuses on the mid-section of the beam. As such, the mesoscale structure and cohesive element models are only utilized near the prefabricated crack in the mid-section of the beam, while the remaining parts of the beam are modeled using a homogeneous material that reflects the elastic response of concrete. To mitigate the effect of mesh size on simulation results, informed by prior findings (Li and Guo 2019; Omar et al. 2022; Baktheer et al. 2024), the element size in all mesoscopic parts of the model was set to 2 mm, and 20 mm in other parts. Some scholars have calibrated the parameters based on the macroscopic mechanical properties of concrete derived from laboratory experiments, achieving relatively ideal simulation outcomes (Malachanne et al. 2018; Zhou et al. 2021; Huang et al. 2022). In this study, concrete with a uniaxial compressive strength of 30 MPa is used as an example. And the volumetric fraction of the aggregate, determined based on the mix ratio, is calculated to be 0.68. Referencing previous study from Zhou (Zhou et al. 2021), the material properties adopted of the FDEM model are listed in Table 1, where M_{agg} , M_{ITZ} , and M_{mortar} respectively denote the properties of interface components for aggregate, ITZ, and mortar.

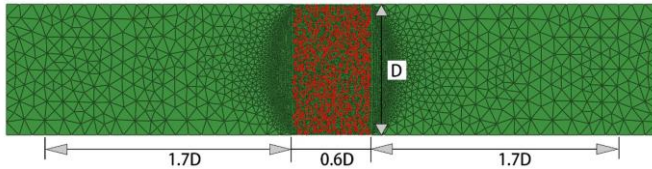


Fig. 4 Mesoscale FDEM model of concrete beam

Table 1. Parameters for the solid elements and cohesive elements from Zhou (Zhou et al. 2021)

	Aggregate	Mortar	M_{agg}	M_{ITZ}	M_{mortar}
Elastic modulus/GPa	60	30	60	15	30
Density (kg/m ³)	2800	2300	2800	2000	2300
Poisson's ratio	0.2	0.2	-	-	-
Maximum allowable tensile stress (MPa)	-	-	16	2.3	4.7
Maximum allowable shear stress (MPa)	-	-	64	9.2	18.8
Type I fractured energy (N/mm)	-	-	0.08	0.03	0.06
Type II fracture energy (N/mm)	-	-	0.8	0.3	0.6

3. Mechanism of Mesoscopic Fracture

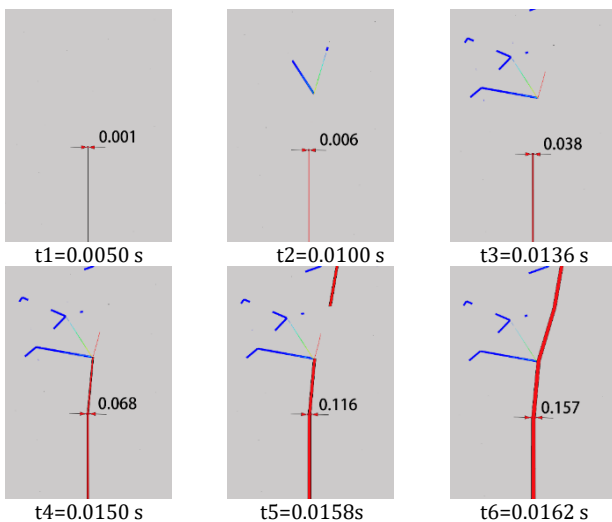


Fig. 5 Forming and evolution of main crack (unit: mm)

The model with a beam depth of 300 mm taken as an example to examine the mesoscopic fracture mechanism of concrete beams under three-point bending load. The process of localized fracture at the tip of the prefabricated crack in the current mesoscopic concrete beam is depicted in Figure 5. As illustrated in Figure 6, Points A and B are in the pre-peak phase, Point C is near the peak load, and Points D, E, and F are in the post-peak phase. The generation of cracks at the fracture tip involves a main crack along with several microcracks. In the pre-peak phase, the main crack is extremely small (at Points A and B). At the peak (Point C), the crack width significantly increases, reaching 0.038 mm. At Point D, the crack begins to extend, and at this point, the load curve starts to decline rapidly.

By Point E, main microcracks also appear in the mortar. At Point F, the microcracks connect with the initial main crack, forming a wider crack that continues to spread. This simulated process of concrete crack development is consistent with experimental observations made through DIC and X-ray (Bhowmik and Ray 2019; Skarżyński and Teichman 2021).

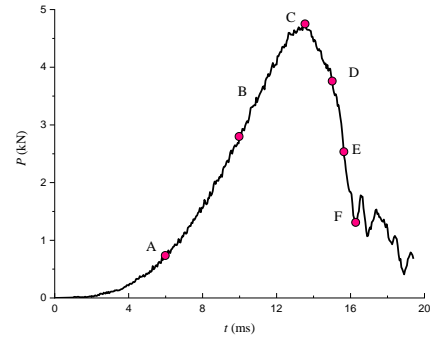


Fig. 6 Load-time curve

Figure 7 presents a contour map of the principal stress evolution in the midspan of the beam, where the stress evolution characteristics within the Fracture Process Zone (FPZ) serve to uncover the fracture mechanisms of concrete. In the initial stages of loading, the overall stress within the beam is relatively low, with no significant stress concentration observed at the tip of the pre-existing crack (Figure 7(a)). As the load increases, a concentration of the principal tensile stress appears near the tip of the pre-existing crack (Figure 7(b)). At the peak load, microcracks begin to form near the ITZ around the tip of the pre-existing crack (Figure 7(c)). As the main crack emerges at the tip of the pre-existing fissure and interconnects with the microcracks at the ITZ, the principal compressive stress at the top of the beam begins to diminish. This indicates the transition of the loading into the post-peak stage. When the crack encounters aggregate particles, its direction of expansion changes, and it meanders along the ITZ propagating upwards (Figure 7(d)). The main crack extends by bridging across the interfaces of microcracks surrounding adjacent aggregates (Figure 7(e)), widening progressively, leading to the beam's near-total loss of load-bearing capacity (Figure 7(f)). Due to the random spatial distribution of aggregates, the path of crack evolution is highly irregular. As the main crack grows, stress concentration occurs near the crack tip, giving rise to many new microcracks, while some of the earlier formed microcracks cease to grow or even close. Furthermore, following cracking, the stresses within the elements are released.

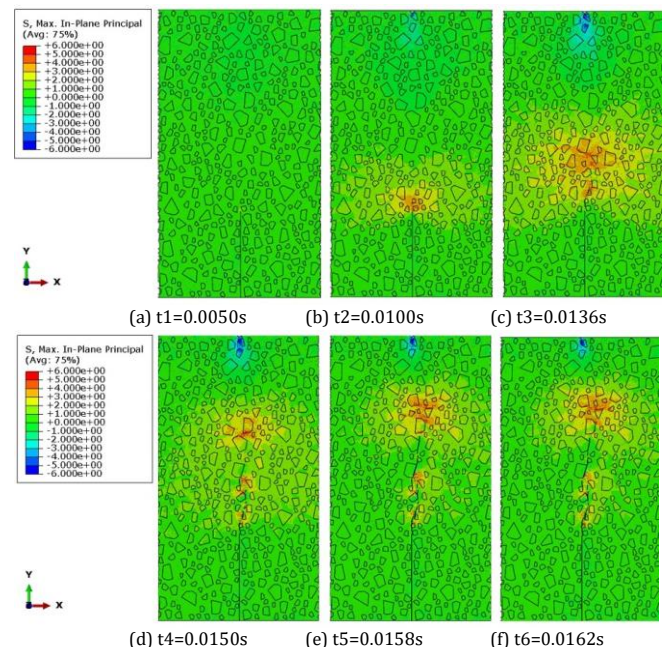


Fig. 7 Evolution of in-Plane principal stress

4. Size effect of concrete fracture characteristics

4.1 P-CMOD curve

The P-CMOD curves obtained from three-point bending simulations of beams with varying depths and notch-to-depth ratio are shown in Figures 8. These results are comparable to the experimental data presented in literature (Karihaloo et al. 2003; Lu and Hu 2015; Chen et al. 2020; Wang

et al. 2021). In Figure 8 (a), the notch-to-depth ratio of the beam models consistently 0.3, while the beam depths are 50 mm, 100 mm, 200 mm, 300 mm, and 400 mm, respectively. As the beam height increases, the load P decreases more rapidly in the post-peak phase of the P-CMOD curve, which indicates that the crack extension is faster in large-sized specimens. This may be because in larger specimens, microcracks within the material are more likely to accumulate and interact, which can lead to faster crack propagation and a quicker decrease in load. In Figure 8 (b), the depth of beam models is 300 mm, while the notch-to-depth ratio are 0.1, 0.2, 0.3, 0.4, and 0.5 respectively. The CMOD values corresponding to the peak loads of specimens with different notch-to-depth ratio are similar. This suggests that the initiation of crack propagation is not significantly by the notch geometry. This implies that, regardless of the notch-to-depth ratio, once the crack starts propagating, the material's resistance to fracture reaches a similar threshold, leading to comparable CMOD values at peak load.

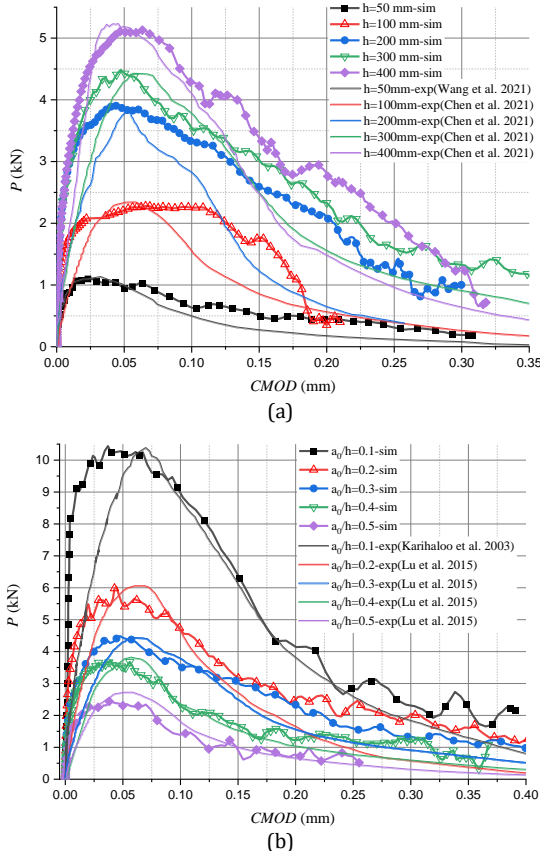


Fig. 8 Comparison of the numerical simulation results of P-CMOD (sim) with the experimental results (exp) in the literature: (a) different depths; (b) different notch-to-depth ratios

4.2 Fracture Toughness

Crack initiation toughness, K_{IC}, is a key material property that represents the material's resistance to crack initiation before the crack reaches an unstable propagation stage. For a three-point bending test, the crack initiation toughness can be calculated using the following formula (Tada et al. 1973; Golewski 2023):

$$K_{IC} = \frac{3PS}{2BD^2} \sqrt{\pi a_0} Y \quad (3)$$

$$Y = \frac{1.99 - \frac{a_0}{D} (1 - \frac{a_0}{D}) (2.15 - 3.93 \frac{a_0}{D} + 2.7 (\frac{a_0}{D})^2)}{\sqrt{\pi (1 + 2 \frac{a_0}{D}) (1 - \frac{a_0}{D})^3/2}} \quad (4)$$

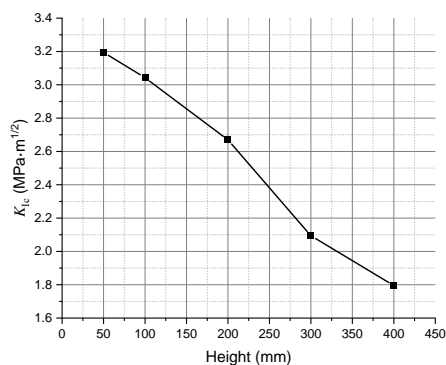


Fig. 9 Variations of fracture toughness with height

Where, P represents the crack initiation load, which is the load applied at the moment the crack begins to propagate. And S is the span length, B is the specimen's thickness, and D denotes the specimen's depth. Additionally, a₀ is the depth of the precast crack, while Y is the geometry correction factor, which is dependent on the crack size.

For three different specimen sizes of concrete beam, the K_{IC} are calculated and shown in Figure 9. The calculated K_{IC} values decrease with increasing specimen size. This indicates that larger specimens exhibit a reduction in crack initiation fracture toughness.

4.3 Fracture Energy and Ductility Index

Fracture Energy (G_f) refers to the energy required to extend a crack over a unit area of the surface and is closely related to the fracture process. It is calculated based on the three-point bending fracture energy formula and the load-deflection (P-δ) curve obtained from the experiment, as shown in equation (5) (Wang et al. 2017). The Ductility Index (D_u) is used to measure the ductility properties of a specimen and is the ratio of Fracture Energy (G_f) to the peak load (P_{max}). The calculation method is provided in equation (6) (Wang et al. 2017).

$$G_f = \frac{W_0}{A_{II}} = \frac{\int_0^{\delta_{max}} P(\delta) d\delta}{B(D-a_0)} \quad (5)$$

$$D_u = G_f / P_{max} \quad (6)$$

Where, W₀ represents the work done by the external load, which is the area enclosed by the P-δ curve and the x-axis. δ_{max} is the maximum opening displacement of the initial crack mouth. A_{II} is the area of the fracture zone of the specimen.

In the post-peak stage of the P-CMOD curve, when the load is reduced to about 1/5 of the peak load, the P-CMOD curve enters a slowly declining phase. And the fracture development slows down afterwards. Therefore, when calculating the fracture energy, only the part before the load drops to 1/5 of the peak load is considered. The simulation data of beam models with different depths are substituted into equations (5) and (6) respectively to calculate their fracture energy and ductility index. The results are plotted in Figure 10.

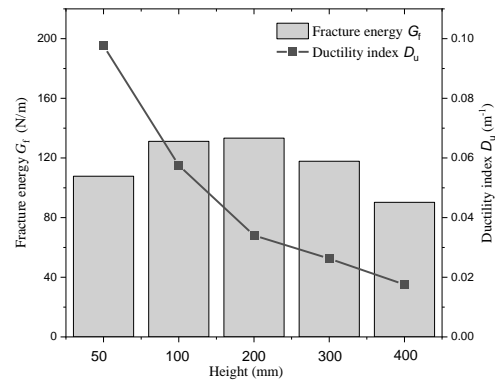


Fig. 10 Variations of fracture energy and ductility index with depth

As the beam depth increases from 50 mm to 400 mm, the fracture energy of the sample shows a trend of first increasing and then decreasing, indicating a certain size effect. It is caused by changes in the effective length ratio of the fracture surface and the uneven distribution of local fractured energy on the fracture ligament. When the beam depth is less than 200 mm, the increase in fracture energy with the increase in beam depth is due to the change in the effective length ratio of the fracture surface; the fracture toughness of the concrete is only related to the properties of the concrete at the tip of the prefabricated fracture. As the depth of the beam increases, the development of the fracture becomes more complete, the fracture process area between the initiation and instability of the beam becomes longer, the effective length ratio of the fracture increases, and the fracture energy increases.

From a macroscopic perspective, the increase in beam depth leads to the crack encountering more aggregates during its initiation and development process. The tortuosity and length of the crack propagation path increase, resulting in the specimen generating more and wider microcracks during the failure process. Thus, the ratio of the actual cracking area to the nominal fracture area is higher. Therefore, the fracture of energy gradually increases as the beam depth increases. However, when the beam depth reaches a certain level, the development of cracks under the load becomes sufficient. The increase in beam depth will no longer affect the effective length ratio of the fracture surface, and thus, the fracture energy no longer increases significantly.

For beams that are taller than 200 mm, the fracture energy slightly decreases as the beam depth increases. This decrease is caused by the uneven distribution of local fractured energy on the fractured ligament. The unevenness of the local fracture energy is due to the localized

differences in the fractured tip elements and the varying constraints at the boundaries. Due to boundary effects, the local constraints on the fracture ligament of larger beams are relatively smaller compared to smaller beams. Therefore, there is a slight decrease in the average fracture of energy. However, it can be anticipated that when the beam depth is sufficiently high, the impact brought by boundary effects can be neglected.

Moreover, as the beam depth increases, the ductility index of the beam gradually decreases, which means that brittleness increases. This may be because the higher the beam, the higher the peak load, and the greater the work done by the load per unit CMOD increases, thereby accelerating the crack propagation and failure of the beam. From a mathematical perspective, as the depth of the beam increases, the peak load continuously increases, while the fracture energy cannot continue to increase. Therefore, as the ratio of the two, the ductility index will continuously decrease, and this trend will not change.

The fracture energy and ductility index obtained from model simulations with different notch-to-depth ratio are shown in Figure 11, where the beam depth of the beam models is uniformly 300 mm. As the notch-to-depth ratio increases, the fracture energy of the beam gradually decreases. This is because for specimens with smaller notch-to-depth ratios, the fracture process zone from initiation to unstable failure is longer, and the tortuosity of cracks generated under the influence of aggregates is greater. Thus, the ratio of the actual length of the crack to the nominal effective length, that is, the effective length ratio of the fracture surface, is larger, resulting in greater fracture energy of the specimen.

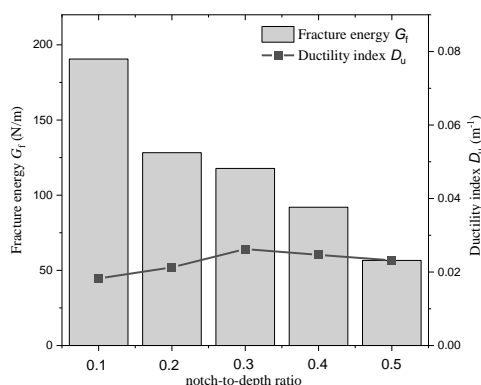


Fig. 11 Variations of fracture energy and ductility index with notch-to-depth ratio

Moreover, when the notch-to-depth ratio is less than 0.3, the ductility index slightly increases with the increase of the notch-to-depth ratio. When the notch-to-depth ratio is greater than 0.3, the ductility index of the specimens no longer changes significantly. On one hand, this is because the presence of precast cracks can lead to a certain degree of stress concentration when the concrete beam is subjected to force. However, when the notch-to-depth ratio is small, the impact of this stress concentration is less, and the range of plastic deformation in the beam is relatively larger. Therefore, the ductility index will slightly increase. However, when the notch-to-depth ratio exceeds a certain value, the plastic deformation capability of the concrete is significantly weakened due to the impact of stress concentration. This is primarily manifested by fractures along the precast cracks, leading to no significant change in the ductility index. On the other hand, this may be due to fluctuations caused by differences in aggregate distribution among different models. Overall, as the notch-to-depth ratio increases, the ductility index of the models all falls within the range of $0.025 \pm 0.0045 m^{-1}$. Compared to changes in the ductility index caused by variations in beam depth, the impact of the notch-to-depth ratio on the beam's ductility index is minimal.

5. Conclusion

This paper has established a micro-scale numerical model of concrete based on the FDEM method. Through the simulation of three-point bending of beams, it has unveiled the micro-fracture process and mechanisms of concrete beams and analyzed the influence patterns of beam depth and different notch-to-depth ratio on the fracture energy and ductility index of concrete. The main conclusions are as follows:

- (1) The generation of cracks at the tip of the void is actually composed of a main crack and numerous micro-cracks. Due to the concentration of the principal tensile stress, the initial major macro-crack appears near the tip of the pre-formed void at the load peak. As the crack begins to extend, the load curve rapidly declines. The crack propagates along the ITZ near the aggregate, extends by bridging the ITZ around adjacent aggregates, and ultimately forms a through crack.
- (2) As the beam height increases, the load P decreases more rapidly in the post-peak phase of the P -CMOD curve, which indicates that

the crack extension is faster in large-sized specimens. Besides, the CMOD values corresponding to the peak loads of specimens with different notch-to-depth ratio are similar. This suggests that the initiation of crack propagation is not significantly influenced by the notch-to-depth ratio.

- (3) The fracture performance of small-scale beams exhibits certain size effects. As the beam depth increases from 50 mm to 400 mm, the fracture toughness of the specimens decreases. And the fracture of energy shows a trend of first increasing and then slightly decreasing. With the increase in the notch-to-depth ratio, the fracture energy of the beams gradually decreases, while the variation in the ductility index is not significant.

Acknowledgements

Thank you for the Key Scientific Research Projects of Universities in Henan Province (23B560005), Henan Science and Technology Research Project (222102320204) and Science and Technology Research Project of China Construction Seventh Engineering Division (JTZB-TJDT-D011/2022) for the support and help provided in this article.

Declaration of Competing Interest

All authors declared no potential conflicts of interest with respect to the research, authorship, and/or publication of this article.

References

- Baktheer, A., E. Martínez-Pañeda, and F. Aldakheel. 2024. "Phase field cohesive zone modeling for fatigue crack propagation in quasi-brittle materials." *Computer Methods in Applied Mechanics and Engineering*, 422: 116834. <https://doi.org/10.1016/j.cma.2024.116834>.
- Bazant, Z. P. 2004. "Probability distribution of energetic-statistical size effect in quasibrittle fracture." *Probabilistic Engineering Mechanics*, 19 (4): 307–319. <https://doi.org/10.1016/j.proengmech.2003.09.003>.
- Bhowmik, S., and S. Ray. 2019. "An experimental approach for characterization of fracture process zone in concrete." *Engineering Fracture Mechanics*, 211: 401–419. <https://doi.org/10.1016/j.engfracmech.2019.02.026>.
- Chen, B., H. Yu, J. Zhang, H. Ma, and F. Tian. 2022. "Effects of the embedding of cohesive zone model on the mesoscopic fracture behavior of Concrete: A case study of uniaxial tension and compression tests." *Engineering Failure Analysis*, 142: 106709. <https://doi.org/10.1016/j.engfailanal.2022.106709>.
- Chen, H., R. K. L. Su, A. S.-L. Folk, and B. Yuan. 2020. "An investigation of fracture properties and size effects of concrete using the ESPI technique." *Magazine of Concrete Research*, 72 (17): 888–899. ICE Publishing. <https://doi.org/10.1680/jmacr.18.00423>.
- Chen, Q., J. Zhang, Z. Wang, T. Zhao, and Z. Wang. 2024. "A review of the interfacial transition zones in concrete: Identification, physical characteristics, and mechanical properties." *Engineering Fracture Mechanics*, 300: 109979. <https://doi.org/10.1016/j.engfracmech.2024.109979>.
- Golewski, G. L. 2023. "The Phenomenon of Cracking in Cement Concretes and Reinforced Concrete Structures: The Mechanism of Cracks Formation, Causes of Their Initiation, Types and Places of Occurrence, and Methods of Detection—A Review." *Buildings*, 13 (3): 765. Multidisciplinary Digital Publishing Institute. <https://doi.org/10.3390/buildings13030765>.
- Guo, X. H., and R. I. Gilbert. 2000. "The effect of specimen size on the fracture energy and softening function of concrete." *Mat. Struct.*, 33 (5): 309–316. <https://doi.org/10.1007/BF02479701>.
- Huang, Y., Z. Yang, H. Zhang, and S. Natarajan. 2022. "A phase-field cohesive zone model integrated with cell-based smoothed finite element method for quasi-brittle fracture simulations of concrete at mesoscale." *Computer Methods in Applied Mechanics and Engineering*, 396: 115074. <https://doi.org/10.1016/j.cma.2022.115074>.
- Karihaloo, B. L., H. M. Abdalla, and Q. Z. Xiao. 2003. "Size effect in concrete beams." *Engineering Fracture Mechanics*, 70 (7): 979–993. [https://doi.org/10.1016/S0013-7944\(02\)00161-3](https://doi.org/10.1016/S0013-7944(02)00161-3).
- Li, C., and J. Guo. 2019. "Cracking simulation of asphalt concrete beam specimen using cohesive zone model." *Construction and Building Materials*, 214: 49–60. <https://doi.org/10.1016/j.conbuildmat.2019.04.122>.
- Liu, F., C. Zhou, B. Wang, Z. Chen, and C. Fan. 2024. "Understanding the interface fracture mechanism by composite BFPMP mortar and cement concrete bending beam." *Journal of Building Engineering*, 95: 110145. <https://doi.org/10.1016/j.job.2024.110145>.
- Lu, W. Y., and S. W. Hu. 2015. "Effect of large crack-depth ratio on three-point bending concrete beam with single edge notch." *Materials Research Innovations*, 19 (sup8): S8-312-S8-317. Taylor & Francis. <https://doi.org/10.1179/1432891715Z.0000000001692>.

- Ma, H., W. Xu, and Y. Li. 2016. "Random aggregate model for mesoscopic structures and mechanical analysis of fully-graded concrete." *Computers & Structures*, 177: 103–113. <https://doi.org/10.1016/j.compstruc.2016.09.005>.
- Malachanne, E., M. Jebli, F. Jamin, E. Garcia-Diaz, and M.-S. El Youssoufi. 2018. "A cohesive zone model for the characterization of adhesion between cement paste and aggregates." *Construction and Building Materials*, 193: 64–71. <https://doi.org/10.1016/j.conbuildmat.2018.10.188>.
- Omar, Z., S. Sugiman, M. M. Yusoff, and H. Ahmad. 2022. "Predicting the Flexural Behaviour of CFRP-Strengthened Concrete Beam using Combined XFEM and Cohesive Zone Model." *J. Appl. Sci. Eng.*, 25 (6): 1077–1090. Tamkang University Press. [https://doi.org/10.6180/jase.202212.25\(6\).0003](https://doi.org/10.6180/jase.202212.25(6).0003).
- Skarżyński, Ł., and J. Tejchman. 2021. "Investigations on fracture in reinforced concrete beams in 3-point bending using continuous micro-CT scanning." *Construction and Building Materials*, 284: 122796. <https://doi.org/10.1016/j.conbuildmat.2021.122796>.
- Tada, H., P. C. Paris, and G. R. Irwin. 1973. "The stress analysis of cracks." *Handbook*, Del Research Corporation, 34 (1973).
- Tang, Y., H. Chen, and J. Xiao. 2022. "Size effects on the characteristics of fracture process zone of plain concrete under three-point bending." *Construction and Building Materials*, 315: 125725. <https://doi.org/10.1016/j.conbuildmat.2021.125725>.
- Wang, Q., H. Chen, H. Zhang, C. Liu, Y. Zhao, and X. Huang. 2017. "Relationship of deflection and crack mouth opening displacement of concrete beams under the three-point bending." *Yingyong Lixue Xuebao/Chinese Journal of Applied Mechanics*, 34 (5): 937–943. <https://doi.org/10.11776/cjam.34.05.D076>.
- Wang, Q., and Y. Xu. 2024. "Macro-meso cracking inversion modelling of three-point bending concrete beam with random aggregates using cohesive zone model." *Theoretical and Applied Fracture Mechanics*, 133: 104566. <https://doi.org/10.1016/j.tafmec.2024.104566>.
- Wang, Z., J. Gou, and D. Gao. 2021. "Experimental Study on the Fracture Parameters of Concrete." *Materials*, 14 (1): 129. Multidisciplinary Digital Publishing Institute. <https://doi.org/10.3390/ma14010129>.
- Wu, Z., H. Rong, J. Zheng, F. Xu, and W. Dong. 2011. "An experimental investigation on the FPZ properties in concrete using digital image correlation technique." *Engineering Fracture Mechanics*, 78 (17): 2978–2990. <https://doi.org/10.1016/j.engfracmech.2011.08.016>.
- Xue, Y., Y. Cheng, Q. Li, K. Wang, W. Xu, and W. Du. 2023. "Research on dynamic failure mechanism of three-point bending beam with joint." *Mechanics of Advanced Materials and Structures*, 30 (4): 870–893. Taylor & Francis. <https://doi.org/10.1080/15376494.2022.2028041>.
- Yankelevsky, D. Z. 2024. "The uniaxial compressive strength of concrete: revisited." *Mater Struct*, 57 (6): 144. <https://doi.org/10.1617/s11527-024-02422-x>.
- Yin, Y., and S. Hu. 2021. "Effects of span-depth ratios on the energy release rate for three-point bending beams." *Engineering Fracture Mechanics*, 244: 107567. <https://doi.org/10.1016/j.engfracmech.2021.107567>.
- Yin, Y., S. Hu, C. Liang, and Y. Sun. 2023. "Crack extension resistance for a general three-point bending concrete beam." *Engineering Fracture Mechanics*, 290: 109490. <https://doi.org/10.1016/j.engfracmech.2023.109490>.
- Yin, Y., Z. Jing, S. Hu, C. Liang, G. Hou, Y. Sun, and Y. Wang. 2024. "Study on crack propagation behaviors of three-point bending concrete beams with small span-depth ratios." *Theoretical and Applied Fracture Mechanics*, 133: 104638. <https://doi.org/10.1016/j.tafmec.2024.104638>.
- Zhang Ruilin, Huang Feng, Deng Shiling, and Liu Xingchen. 2023. "Simulation of Crack Propagation of Concrete Pure Bending Beam Based on XFEM." *Chinese Quarterly of Mechanics*, 44 (1): 193–202. <https://doi.org/10.15959/j.cnki.0254-0053.2023.01.019>.
- Zhou, R., and H.-M. Chen. 2019. "Mesoscopic investigation of size effect in notched concrete beams: The role of fracture process zone." *Engineering Fracture Mechanics*, 212: 136–152. <https://doi.org/10.1016/j.engfracmech.2019.03.028>.
- Zhou, R., H.-M. Chen, and Y. Lu. 2020. "Mesoscale modelling of concrete under high strain rate tension with a rate-dependent cohesive interface approach." *International Journal of Impact Engineering*, 139: 103500. <https://doi.org/10.1016/j.ijimpeng.2020.103500>.
- Zhou, R., Y. Lu, L.-G. Wang, and H.-M. Chen. 2021. "Mesoscale modelling of size effect on the evolution of fracture process zone in concrete." *Engineering Fracture Mechanics*, 245: 107559. <https://doi.org/10.1016/j.engfracmech.2021.107559>.
- Zhu, S., Z. Zhou, and Y. Xiong. 2024. "Mesoscale fracture analysis of three-point bending concrete beams based on cohesive zone model." *Engineering Fracture Mechanics*, 296: 109828. <https://doi.org/10.1016/j.engfracmech.2023.109828>.

Disclaimer

The statements, opinions and data contained in all publications are solely those of the individual author(s) and contributor(s) and not of EJSEI and/or the editor(s). EJSEI and/or the editor(s) disclaim responsibility for any injury to people or property resulting from any ideas, methods, instructions or products referred to in the content.